PCCP



View Article Online **PAPER**



Cite this: Phys. Chem. Chem. Phys., 2024, 26, 20672

Received 13th February 2024, Accepted 11th June 2024

DOI: 10.1039/d4cp00637b

rsc.li/pccp

Unveiling the photophysical and excited state properties of multi-resonant OLED emitters using combined DFT and CCSD method†

Multi-resonance thermally-activated delayed fluorescence (MR-TADF) is predominantly observed in organoboron heteroatom-embedded molecules, featuring enhanced performance in organic lightemitting diodes (OLEDs) with high color purity, chemical stability, and excellent photoluminescence quantum yields. However, predicting the impact of any chemical change remains a challenge. Computational methods including density functional theory (DFT) still require accurate descriptions of photophysical properties of MR-TADF emitters. To circumvent this drawback, we explored recent investigations on the CzBX (Cz = carbazole, X = O, S, or Se) molecule as a central building block. We constructed a series of MR-TADF molecules by controlling chalcogen atom embedding, employing a combined approach of DFT and coupled-cluster (CCSD) methods. Our predicted results for MR-TADF emitter molecules align with the reported experimental data in the literature. The variation in the positions of chalcogen atoms embedded within the CzBX2X framework imparts unique photophysical properties.

1. Introduction

In recent years, pure organoboron molecules with heteroatoms are attractive candidates that are receiving considerable attention and are a hot topic of research because of their narrowband emissive property, purity of color, and versatile applications in fields such as optoelectronic devices, photocatalytic synthesis, quantum information technologies, and organic light-emitting diodes (OLEDs). 1-8 Researchers are particularly focused on the characteristics of triplet excited states to enhance the luminescence efficiency. 9-16 The conversion between singlet and triplet states occurs through intersystem crossing (ISC) and reverse intersystem crossing (RISC), respectively, with these processes playing a pivotal role in achieving a high quantum yield for the luminescence process. 17-19 Efficient ISC and RISC processes efficiently occur for low energy gap $(\Delta E_{\rm ST})$ between the lowest excited singlet (S_1) and the lowest

excited triplet energy (T_1) states. $\Delta E_{\rm ST} < \sim 0.3$ eV promotes the molecule's role as a thermally-activated delayed fluorescence (TADF) emitter. The TADF mechanism involves the thermal up-conversion of triplet excitons into singlets via RISC. 19-23 Conversely, if $\Delta E_{\rm ST}$ exceeds ~0.4 eV, delayed luminescence at room temperature is most likely due to the room temperature phosphorescence (RTP) and triplet-triplet annihilation (TTA). 24-29 Rate constants for RISC (k_{RISC}) and ISC (k_{ISC}) are intrinsic characteristics dependent on their electronic structure and configuration of molecules. The interplay between the lowest energy gap (ΔE_{ST}) and high spin-orbit coupling (SOC) between the singlet and triplet excited states are two important factors that determine the path for the RISC and ISC processes. To harvest the lowest excited states (i.e., ISC for $S_1 \rightarrow T_n$ and RISC for $T_1 \rightarrow S_1$ conversion), a strong SOC matrix element (SOCME) is essential. In the case of MR-TADF, the rate of RISC is a key factor for efficiently harvesting triplet excitons and thereby converting them into radiative singlet excitons to achieve an internal quantum efficiency (IQE) of $\sim 100\%$. In some rare cases of MR-TADF molecules, where the S₁ state energy is close to the energies of two triplets (T1 and T2) with a low $\Delta E_{\mathrm{S_1-T}_n} < 0.25$ eV, the $\mathrm{T_1}$ exciton can also be harvested viaRISC from $S_1 \leftarrow T_2$.³² Hatakeyama *et al.* observed MR-TADF features in DABNA derivatives containing boron and nitrogen atoms. 33 Although the k_{RISC} was initially slow, it was improved significantly in recently developed MR-TADF materials. 9,34-37 A narrow full-width at half-maximum (FWHM) of less than 35 nm is beneficial for enhancing the spectral purity.³⁸⁻⁴⁰

^a Department of Chemistry, Birla Institute of Technology and Science (BITS) Pilani, Hyderabad Campus, Hyderabad-500078, India.

E-mail: pralokkumar.samanta@hyderabad.bits-pilani.ac.in, pralok.samanta@gmail.com

^b Department of Chemistry, School of Science, GITAM University, Hyderabad-502329, India

[†] Electronic supplementary information (ESI) available: STEOM-DLPNO-CCSD computational details, structural details, excited state energy using different DFT functional, HOMO, LUMO, ΔE_{H-L} , configurations percentage, and calculated fluorescence and phosphorescence rate constants (pdf). See DOI: https://doi. org/10.1039/d4cp00637b

Extending the molecule (donor-acceptor) or introducing substitution (heavy atoms) gradually increases the performance and reduces the FWHM value. 38-40 Recent studies by Park et al. explored organoboron emitters doped with chalcogens to enhance the MR-TADF property for achieving excellent color purity and high luminescence efficiency. 41 Using the design concept by Hatakeyama et al., featuring the MR effects as a new approach to the development of narrowband TADF emitters. MR-TADF molecules used polyaromatic compounds based on organoboron.33 Hatakeyama and others have introduced a new strategy for the design of embedding methods in organoboronbased polyaromatic molecules. 42-45 Organoboron-based polyaromatic adjacent phenyl units have two hydrogen bonds converted to a heavy atom or chalcogen atom bond in MR-TADF molecules, and this type of embedded molecule shows excellent performance in OLEDs. 34,44-46 Moreover, Park et al. identified a novel ideal superimposed fluorescence mechanism for the CzBSe molecule, exhibiting a high k_{RISC} up to $\sim 10^8 \text{ s}^{-1}$. The k_{RISC} significantly increases with an upsurge in the chalcogen atomic number $(9.0 \times 10^3, 4 \times 10^5 \text{ and } 1.5 \times 10^8 \text{ s}^{-1} \text{ for O, S and})$ Se, respectively) in toluene solvent.⁴¹ In this article, we unravel the photophysical properties of the recently published CzBX (X = O, S, or Se) molecules and successfully reproduced the experimental data with the combined DFT and CCSD approach results. 47,48 The chalcogen-embedded framework for CzBX2X molecules significantly improved the narrowband emission and optical properties. In addition to that, we investigated a comparative study of the MR-TADF CzBX skeleton molecules: CzBO (5-oxa-8b-aza-15bborabenzo[a]naphtho[1,2,3-hi]aceanthrylene), CzBS (5-thia-8baza-15b-borabenzo[a]naphtho[1,2,3-hi]aceanthrylene) and CzBSe (5-selena-8*b*-aza-15*b*-borabenzo[*a*]naphtho[1,2,3-*hi*]aceanthrylene). We also proposed and calculated the photophysical and excited properties of a series of CzBX2X-type MR-TADF molecules by controlling chalcogen atom embedding: CzBO2O (6,10,13trioxa-3a2-aza-5a2-boraindeno[1,2,3,4-pqra]naphtho[3,2,1,8-ghij]perylene), CzBO2S (10-oxa-6,13-dithia-3a2-aza-5a2-boraindeno-[1,2,3,4-pqra]naphtho[3,2,1,8-ghij]perylene), CzBO2Se (10-oxa-6,13-diselena-3a2-aza-5a2-boraindeno[1,2,3,4-pqra]naphtho[3,2,1, 8-ghij perylene), CzBS2O (6,13-dioxa-10-thia-3a2-aza-5a2-boraindeno[1,2,3,4-pqra]naphtho[3,2,1,8-ghij]perylene), CzBS2S (6,10,13trithia-3a2-aza-5a2-boraindeno[1,2,3,4-pqra]naphtho[3,2,1,8-ghij]perylene), CzBS2Se (10-thia-6,13-diselena-3a2-aza-5a2-boraindeno[1,2,3,4-pqra]naphtho[3,2,1,8-ghij]perylene), CzBSe2O (6,13dioxa-10-selena-3a2-aza-5a2-boraindeno[1,2,3,4-pqra]naphtho-[3,2,1,8-ghij]perylene), CzBS2S (6,13-dithia-10-selena-3a2-aza-5a2-boraindeno[1,2,3,4-pqra]naphtho[3,2,1,8-ghij]perylene) and **CzBSe2Se** (6,10,13-triselena-3*a*2-aza-5*a*2-boraindeno[1,2,3,4-*pqra*]naphtho[3,2,1,8-ghij]perylene) (see Fig. 1).

2. Theoretical methodology and computational details

2.1 Geometries optimization and optical absorption

Ground state (S₀) optimizations were carried out using density functional theory (DFT) employing the optimally tuned

screened range-separated hybrid (OT-SRSH)^{15,49,50} ωB97XD functional (ω values are listed in Table S1a, ESI†) and 6-31G(d) basis set for H, B, C, N, O and S atoms except for Se atom, for which the ECP (effective core potential) type basis set LANL2DZ was used. Excited state geometry optimizations were performed using time-dependent DFT (TDDFT) method with OT-SRSHωB97XD functional with the abovementioned basis set. The toluene solvent was modeled with polarizable continuum model (PCM) with dielectric constant (ε) = 2.3741 to compare with the reported experimental data available in the literature.⁵¹ For TDDFT calculations, Tamm-Dancoff approximation (TDA) were considered to avoid triplet instability. 49 The range-separation parameter, ω for OT-SRSH- ω B97XD functional was determined by minimizing J^2 as follows. $^{52-54}$

$$J^{2} = \sum_{i=0}^{1} |\varepsilon_{H}(N+i) + IP(N+i)|^{2}$$
 (1)

where IP and ε_H denote the ionization potential and HOMO (highest occupied molecular orbital) energy of a given molecule, respectively, and N is the number of electrons in the molecule. All the DFT and TDDFT calculations mentioned above were carried out with the Gaussian 16 software. 55 In a previous study, Olivier and coworkers showed that linear-response DFT approaches consistently overestimate the ΔE_{ST} gaps in MR-TADF molecules.56 We carried out similarity transformed equation-ofmotion coupled-cluster (with single and double excitations) method augmented with domain-based on local pair natural orbitals (STEOM-DLPNO-CCSD), which is a highly correlated wave function-based approach. It offers an accurate treatment for the excited state characteristics of various molecules, including MR-TADF molecules. These wavefunction-based calculations were performed with def2-TZVP basis set, as implemented in the ORCA V5.0.3 package. 57,58 To avoid prohibitive computational costs, the energies of the singlet and triplet states and the related $\Delta E_{\rm ST}$ values were calculated using STEOM-DLPNO-CCSD/def2-TZVP on the basis of the excited-state geometries (for S₁, T₁ and T₂) obtained using the OT-SRSH-ωB97XD/6-31G(d)/LANL2DZ level of theory. This protocol provides manageable computational costs, while accurately reproducing the experimental data reported for known MR-type molecules. 59,60 Thus, in our combined DFT and CCSD method, we used the OT-SRSH-\(\omega\)B97XD/ 6-31G(d)/LANL2DZ level of theory for geometry optimization and STEOM-DLPNO-CCSD/def2-TZVP level of theory for single-point energy calculation. Vertical excitation calculation of STEOM-DLPNO-CCSD configuration details is provided in the ESI.†

2.2 Intersystem crossing (ISC) rate

The rate constant for the ISC process from $S_1 \rightarrow T_n$ conversions and RISC process from T_1 or $T_2 \rightarrow S_1$ conversions were calculated using the Fermi's Golden Rule^{61,62}

$$k_{\rm ISC/RISC}^{n} = \frac{2\pi}{\hbar} \rho_{\rm FC} \left| \left\langle S_1 \middle| \hat{H}_{\rm SOC} \middle| T_n \right\rangle \right|^2 \tag{2}$$

where $\langle S_1 | \hat{H}_{SOC} | T_n \rangle$ and ρ_{FC} denote the spin-orbit coupling matrix element (SOCME) between the S_1 and T_n state and Franck-Condon weighted density of states, respectively. We used

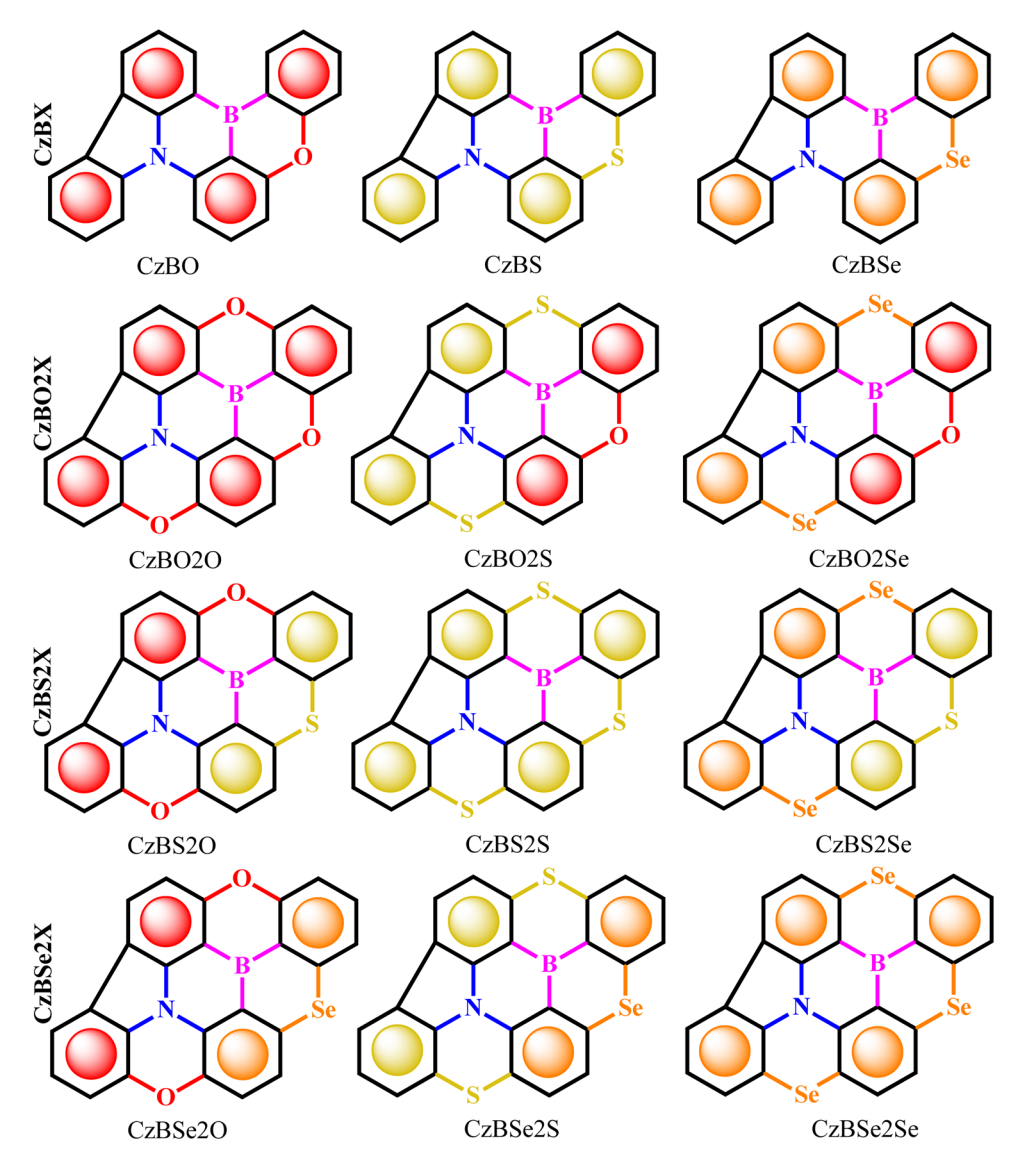


Fig. 1 Chemical structures of the CzBX and CzBX2X series are investigated in this work where X = O, S and Se. CzBX molecules are experimentally reported before, and CzBX2X molecules are proposed in this work.

optimized excited state geometry (T1, T2-state optimized geometry for RISC and S₁ state optimized geometry for ISC) obtained using $OT\text{-}SRSH\text{-}\omega B97XD/6\text{-}31G(d)/LANL2DZ//STEOM\text{-}DLPNO\text{-}CCSD/$ def2-TZVP (DFT-CCSD) for the calculation of the SOCME between the S₁, T₁ and T₂ states. According to the Franck-Condon principle, electronic transition happens first and then relaxation of the geometry occurs. Thus, we considered the T_1 , T₂-state optimized geometry for the calculation of the SOCME between the S₁ and T₁, and S₁ and T₂ states as we studied the transition (i.e., ISC and RISC) from the T1, T2 state to S1 state (RISC), and S_1 state to T_1 , T_2 state (ISC). The ρ_{FC} was estimated using the Marcus-Levich-Jortner theory.⁶³

$$\rho_{FC} = \frac{1}{\sqrt{4\pi\lambda_{M}k_{B}T}} \sum_{n=1}^{\infty} \exp(-S) \frac{S^{n}}{n!} \exp\left[-\frac{(\Delta E_{ST} + n\hbar\omega + \lambda_{M})^{2}}{4\lambda_{M}k_{B}T}\right]$$
(3)

where $\lambda_{\rm M}$ is the reorganization energy, $k_{\rm B}$ is the Boltzmann constant, T is the absolute temperature, S is the effective Huang-Rhys factor (S) associated with non-classical highfrequency intramolecular vibrational modes, and we found that S is less than 0.05 and the RMSD is less than 0.04 Å between the S₁ and T₁ optimized geometries. Thus, the reorganization energy between the S_1 and T_1 optimized geometries tends to zero (see Table S1b, ESI†). Thus, the S values were considered to be zero. The total reorganization energy has two components: the intramolecular reorganization energy is ~ 0.006 eV (see Table S1c, ESI†) and the contribution of reorganization energy from the surroundings and solvent effect approximated to 0.2 eV. It is worthy to note that $\Delta E_{\rm ST} = \Delta E_{\rm S,-T_n}$ for the ISC process whereas $\Delta E_{\rm ST} = \Delta E_{\rm T_n-S_1}$ for the RISC process. We used our own FORTRAN code to calculate $k_{\rm RISC/ISC}$ using eqn (2) and (3) (available on https://Github.-Com/Pralok87/Fortran-Code-for-ISC (https://Github.Com/Pra lok87/Fortran-Code-for-ISC)). The overall intersystem crossing

Paper

rate constant (k_{ISC}) from the excited S_1 state to the triplet manifold (T_m) is given by 63

$$k_{\rm ISC} = \sum_{m} k_{\rm ISC}^{m} \tag{4}$$

Fluorescence and phosphorescence rate

The fluorescence and phosphorescence calculations were done based on excited state geometries optimized using the OT-SRSH-ωB97XD/6-31G(d)/LANL2DZ method. In order to account for the solvent effect, the toluene conductor-like polarizable continuum model (CPCM) was used. The fluorescence rate constants (k_r) were calculated using Einstein A coefficient ^{63,64}

$$k_{\rm r} = A_{\rm fi} = \frac{\left(E_f - E_i\right)^3}{3\varepsilon_0 \pi \hbar^4 c^3} |\langle f|\hat{\mu}|i\rangle|^2 \tag{5}$$

where E_f and E_i are the energies of the excited (f) and ground states (i), respectively, and $f|\hat{\mu}|i$ is the corresponding transition– dipole moment.

The phosphorescence rate constant, $k_{\rm ph}$ and radiative lifetime $\tau_{\rm ph}$ from each sublevel i (i = I, II, III) of the T_1 state to the ground S₀ state were calculated by making use of the transition energy ΔE_i and the transition dipole moment M_i , as defined in egn (6)65,66

$$k_{i} = \frac{1}{\tau_{i}} = \frac{4}{3t_{0}} \alpha_{0}^{3} (\Delta E_{i})^{3} \sum_{\alpha = \chi, \nu, z} |M_{\alpha}^{i}|^{2}$$
 (6)

where $t_0 = (4\pi\varepsilon_0)^2 \hbar^3 / m_e e^4$. ε_0 , \hbar , m_e , e and α_0 are the vacuum permittivity, reduced Planck constant, electron mass, electron charge and the fine structure constant, respectively. The contribution to the transition moment was calculated from the first-order (higher order is neglected in this study) corrected wave functions. The sublevels of the triplet state are considered to be energy degenerate; thus, the final expression for M_{α}^{i} is

$$M_{\alpha}^{i} = \sum_{n=0}^{\infty} \frac{\langle \mathbf{S}_{0} | \hat{\mu}_{\alpha} | \mathbf{S}_{n} \rangle \langle \mathbf{S}_{n} | \hat{H}_{SOC} | \mathbf{T}_{1}^{i} \rangle}{E(\mathbf{S}_{n}) - E(\mathbf{T}_{1})} + \sum_{n=1}^{\infty} \frac{\langle \mathbf{S}_{0} | \hat{H}_{SOC} | \mathbf{T}_{n} \rangle \langle \mathbf{T}_{n} | \hat{\mu}_{\alpha} | \mathbf{T}_{1}^{i} \rangle}{E(\mathbf{T}_{n}) - E(\mathbf{S}_{0})}$$
(7)

The transition dipole moment operator $\hat{\mu}$ can be expanded in terms of vibrational normal modes.^{67,68}

$$\widehat{\mu(Q)} = \widehat{\mu_0} + \sum_{k} \left(\frac{\partial \widehat{\mu}}{\partial Q_k} \right)_{Q_k = 0} Q_k + \mathcal{O}(Q_k^2)$$
 (8)

The first order correction term (i.e., the Herzberg-Teller (HT) term) was taken into account in eqn (8) as it can significantly impact the spectra and rate constant calculations.⁶⁹ For the calculation of $k_{\rm F}$ and $k_{\rm ph}$, we considered the adiabatic hessian (HESSFLAG AH) method along with the Cartesian coordinate systems using the excited state dynamics (ESD) module of the ORCA package. 68,70 A broadening parameter of 200 cm⁻¹ was used. Both the emission calculations were done using the OT-SRSH-ωB97XD and def2-TZVP basis set as implemented in the ORCA V5.0.3 package.⁵⁸

We note that the computational methodology used here works relatively well as we compared our calculated results

with the available experimentally reported data. The harmonic approximation to the vibrational normal modes works well for the calculation of radiative rate constant, but it is more prone to errors for the calculation of non-radiative rate constants.⁶⁸ However, the approximation works well for present molecules due to the less structural relaxation of their ground and excited states optimized geometries. Also, the PCM solvent (toluene) model was used to mimic the surrounding environment effect in the bulk. As the properties of any thin film depends on its thickness, it is difficult to mimic the properties of thin films in reality.

Results and discussion

Structural and electronic properties

The optimized geometrical parameter of the ground-state (S_0) shows the accuracy of the experimental molecule nature. The bond lengths and angles of CzBX (X = O, S, or Se) molecules well match with that of the experimental single crystal structure (CIF).41 The bond lengths of carbon and chalcogen atoms (C-X, X = O, S, Se) are 1.37, 1.75 and 1.90 Å, as reported in the experimental study, and are well comparable with our predicted results of 1.36, 1.77 and 1.89 Å, respectively. The bond lengths between the boron and carbon (C-B) bonds are $\sim 1.54-1.56$ Å. The distance between the carbon and nitrogen (C-N) atoms ~ 1.40 –1.43 Å and are well comparable with the reported experimental data (see Table 1 and Fig. 2). The angle of CXC, CBC and CNC decreased correspondingly to the chalcogen atoms.

The HOMO and LUMO (lowest unoccupied molecular orbital) energy levels and their associated ΔE_{H-L} help to explain the origins of the energy shifts of the singlet and triplet states upon the substitution of O, S and Se. In CzBX-type molecules, both the HOMO and LUMO energies decrease in the order O, S and Se $(E_{\text{HOMO}} = -7.537, -7.421 \text{ and } -7.408 \text{ eV}; E_{\text{LUMO}} = 1.183,$ 1.111 and 1.081 eV, respectively, see Table S2, ESI†). The HOMO and LUMO gap (ΔE_{H-L}) decreases in the same order (8.720, 8.532 and 8.489 eV for O, S and Se, respectively). It is the reason behind the red shift in the S₁ and T₁ energies going from O to S and Se for CzBX molecules (see Fig. 3). The results can be explained from the electronegativity of the chalcogen atoms. A similar observation was found for doubly substituted chalcogens CzBX2X series, following the same trend (see Table S2, ESI†).

3.2 Excited state optical properties

The calculated photophysical properties of the CzBX molecules are compared with the available experimental data (see Table 2). The UV-visible absorption spectrum calculated for the CzBX molecules exhibits a characteristic spectral signature with the lowest energy absorption maximum (λ_{abs}^{max}) in the range of 422-450 nm. For the CzBO molecule, the calculated λ_{abs} is 422 nm (f = 0.3415), which is well comparable with the experimental results (λ_{abs} is 426 nm). On the other hand, the calculated λ_{abs}^{max} for S and Se substituted for the CzBS molecules

 $\textbf{Table 1} \quad \text{Comparison data from the experimental single crystal structure and theoretically optimized (OT-SRSH-ωB97XD/6-31G(d)/LANL2DZ) geometry (OT$

Molecules	$C-X^a$	$C-X^b$	$C-B^c$	$\mathrm{C}\mathrm{B}^d$	$C-N^e$	$C-N^f$	CXC^g	CBC^h	CBC^i	CNC^j	CNC^k
Expt. ⁴¹											
CzBO	1.37	1.38	1.54	1.55	1.41	1.43	122.2	114.7	130.6	121.5	130.5
CzBS	1.75	1.75	1.55	1.56	1.41	1.42	106.8	114.1	125.6	121.2	130.6
CzBSe	1.90	1.90	1.54	1.54	1.41	1.43	101.8	113.9	123.9	120.7	129.9
Calculated res	sults										
CzBO	1.36	1.37	1.53	1.55	1.40	1.41	122.7	114.6	130.7	121.6	130.2
CzBS	1.77	1.77	1.55	1.55	1.40	1.41	106.0	114.4	125.7	121.2	130.3
CzBSe	1.89	1.89	1.55	1.55	1.40	1.41	102.6	114.2	124.2	121	130.4

^a Carbon and chalcogen atom distance. ^b Carbon and chalcogen atom distance. ^c Carbon and boron atom distance. ^d Carbon and boron atom distance. ^e Carbon and nitrogen atom distance. ^f Carbon and nitrogen atom distance. ^g Angle of carbon, chalcogen and carbon atoms. ^h Angle of carbon, boron and carbon atoms. ^l Angle of carbon, nitrogen and carbon atoms. ^k Angle of carbon, nitrogen and carbon atoms. Distances are given in Å and angles are given in degrees. See Fig. 2 for angles and distances mentioned in footnotes a-k.

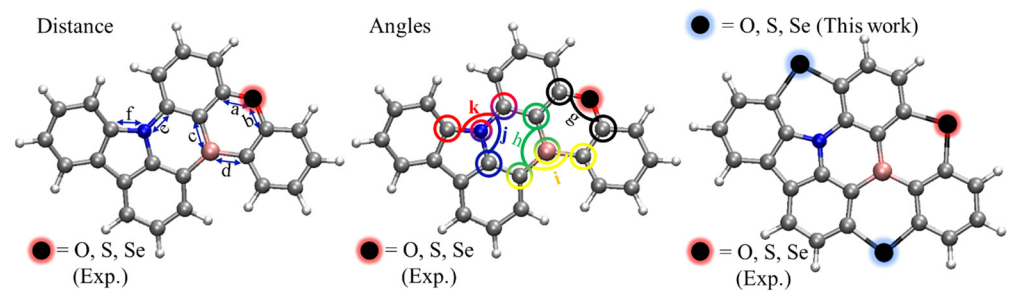


Fig. 2 Chemical structures of the CzBX: left distances, middle angles of CzBX, and right substitution of chalcogen (CzBX2X) atoms (X = O, S, or Se), see Table 1.

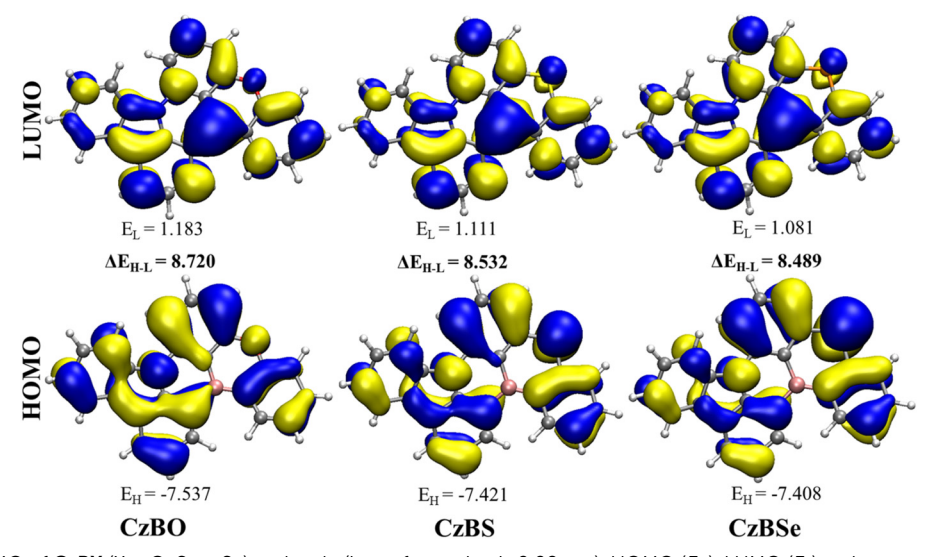


Fig. 3 HOMO and LUMO of CzBX (X = O, S, or Se) molecule (isosurface value is 0.02 a.u.). HOMO (E_H) , LUMO (E_I) and energy gap (ΔE_{H-1}) energies are given in eV (obtained from the combined DFT-CCSD method).

are 441.8 nm (f = 0.3169) and 450.0 nm (f = 0.2881), respectively. This result is well comparable to the reported experimental values for CzBX (447 nm and 451 nm for S and Se substitution, respectively). These results show the importance of the combined DFT and CCSD method used in this work (see Table 2). Orbital configurations of the transitions are provided

in Table S3 (ESI†). The combined DFT and CCSD method effectively reproduces the fluorescence data of the CzBX molecules. The calculated (experimental) fluorescence energies are 446.4 (445) nm, 468.3 (471) nm, and 476 (477) nm, respectively for O, S and Se substituted CzBX molecules, respectively (see Table 3).

Calculated low energy optical absorption (in eV) spectra compared with different functionals and the experimental reported results (ref. 41)

Molecules	Expt. ⁴¹	B3LYP	BHandHLYP	CAM-B3LYP	M062X	PBE0	ωb97xD	ω*B97XD	Combined DFT and CCSD	
CzBO	2.910	3.036 f = 0.330	3.625 f = 0.488	3.520 f = 0.488	3.489 f = 0.476	3.138 f = 0.357	3.580 $f = 0.507$	3.427 f = 0.455	2.938 f = 0.342	
CzBS	2.774	2.887 $f = 0.301$	3.476 $f = 0.442$	3.375 $f = 0.413$	3.334 f = 0.394	2.986 f = 0.324	3.435 $f = 0.463$	3.272 $f = 0.413$	2.806 f = 0.317	
CzBSe	2.749	2.810 $f = 0.274$	3.418 $f = 0.412$	3.318 $f = 0.444$	3.270 $f = 0.429$	2.910 $f = 0.296$	3.380 $f = 0.432$	3.210 $f = 0.383$	2.755 $f = 0.288$	
MAD*	0	0.100	0.695	0.593	0.554	0.200	0.654	0.492	0.022	
$*MAD = \sum$	*MAD = $\sum \frac{ \text{Calc.} - \text{Expt.} }{n}$.									

Table 3 Comparison data of experimental (ref. 41) and theoretical absorption, emission profile data using the DFT-CCSD level of theory. f is the oscillator strength

	$\lambda_{\rm abs}$ (S ₀	$\rightarrow S_1$) in nm	$\lambda_{\rm F} \left({\rm S}_1 \rightarrow {\rm S}_0 \right) {\rm in nm}$				
Molecules	Expt.	Cal.	Expt.	Cal.			
CzBO CzBS CzBSe	426 447 451	422.0 (f = 0.3415) 441.8 (f = 0.3169) 450.0 (f = 0.2881)	445 471 477	446.4 (f = 0.2985) 468.3 (f = 0.2803) 476.0 (f = 0.2666)			

3.3 Intersystem crossing and reverse intersystem crossing process

3.3.1 Origin of SOC and intersystem crossing (ISC). The interesting thing about light sources is that SOC depends on the structure, shape of the molecules and heavy atom effect, which will have a significant impact. Nowadays, organic molecule-based MR emitters are mostly constructed with heavy atoms (S, Se, Te and Br) and twisted-shape structures to achieve faster RISC rate constants for fluorescence. Additionally, the $\Delta E_{\rm ST}$ plays a crucial role in fluorescence-based emitters. Both $\Delta E_{\rm ST}$ and SOCME are important components in the overall TADF process. In this work, we explored a series of CzBX (X = O, S, Se) and substituted series of CzBX2X-based emitters. In the CzBX series of molecules, the fluorescence emission and delayed emission are purely dependent upon the puckered shape of the structure, heavy atoms and low $\Delta E_{\rm ST}$. The $\Delta E_{\rm S_1-T_1}$ values decrease with an increase in the atomic number of the chalcogen atoms (0.155, 0.113 and 0.095 eV for O, S and Se-substituted CzBX, respectively). On the other hand, the experimentally reported $\Delta E_{S_1-T_1}$ values are 0.15, 0.11 and 0.12 eV for O, S and Se-substituted CzBX, respectively. The calculated $\Delta E_{S_1-T_1}$ values are well comparable with the reported experimental results (Table 4).

On the other hand, the $\Delta E_{S_1-T_2}$ increases with the chalcogen atom decreasing order (-0.054, -0.146 and -0.173 eV for O, S)and Se-substituted CzBX, respectively). The negative $\Delta E_{S,-T_0}$ value indicates that the T2 state is higher in energy than the S1 state. The $\Delta E_{S_1-T_n}$ energies between the S_1 and T_n (n = 1, 2)states and SOCME are reported in Tables 5 and 6 for the CzBX series. Based on the above $\Delta E_{\rm ST}$ gap, we have calculated the rate constants of two possible transition ISC and RISC processes. Both the ISC and RISC process of MR-TADF emitters are greatly connected with the strength of SOC between the singlet and triplet states. In this study, for both CzBX and CzBX2X series, the strength of SOCME strongly depends on the excited state geometry and the presence of chalcogen atoms. Fig. 4 illustrates the top and side views, depicting the puckered shape for the CzBX series, the umbrella curve shape (UCS) for a few molecules, and the planar shape structure in the CzBX2X series (X = O, S, or Se). Also, the bond lengths (see Table S5, ESI†) increase in the same chalcogen order (O \rightarrow S \rightarrow Se). CzBO $(d(C-O) \text{ is } \sim 1.36-1.37 \text{ Å}), CzBS (d(C-S) \text{ is } \sim 1.75-1.76 \text{ Å}), and$ CzBSe $(d(C-Se) \sim 1.87-1.89 \text{ Å})$ greatly increased this puckered shape structure, which helps to achieve the higher value of SOC matrix elements. For the ISC rate (k_{ISC}) , SOCME is calculated in the geometry of S_1 for the ISC from $S_1 \rightarrow T_n$ (n = 1, 2) states. The SOCME between the S₁ and T₁ states increases with an increase in the atomic number of chalcogen atoms (0.086, 0.381 and 2.495 cm⁻¹ for O, S, and Se-substituted CzBX, respectively). A similar observation was noted for the SOCME between the S₁ and T_2 states for CzBX molecules (0.099, 0.527 and 3.833 cm⁻¹, respectively). For the calculation of the RISC rate constants (k_{RISC}) , the SOCMEs were calculated in the T₁ state optimized geometry for the $T_1 \rightarrow S_1$ RISC process and the T_2 state optimized geometry for the $T_2 \rightarrow S_1$ state RISC process. Similar to the SOCME for the ISC process, the SOCME for the RISC process increases with an increase in the atomic number of

Table 4 Calculated and experimental (ref. 41) $\Delta E_{S_1-T_1}$ (in eV) with different DFT functionals and CCSD methods

Molecules	Expt.	B3LYP	BHandHLYP	CAM-B3LYP	M062X	PBE0	ωb97xD	ω*B97XD	Combined DFT and CCSD
CzBO	$0.15^a, 0.16^b$	0.46	0.87	0.73	0.60	0.51	0.67	0.55	0.155
CzBS	$0.11^a, 0.14^b$	0.46	0.73	0.63	0.57	0.50	0.63	0.51	0.113
CzBSe	$0.12^a, 0.15^b$	0.45	0.62	0.61	0.54	0.49	0.61	0.50	0.095
MAD	0	0.330	0.616	0.528	0.442	0.373	0.512	0.393	0.011

a Experimental values are measured in toluene. Experimental values are measured in film state. The MAD value is calculated with respect to the experimental values obtained in toluene solvent. The tuned ω for ω*B97XD are provided in Table S1 (ESI).

PCCP

Table 5 Calculated singlet-triplet energy difference (ΔE_{ST}), spin-orbit coupling matrix element (SOCME), and ISC rate constants (k_{ISC}) for the CzBX series

$\Delta E_{ m ST}{}^a \ { m (eV)}$		SOCME ^a (c	em ⁻¹)	$k_{\rm ISC} (s^{-1})$		Expt. [ref. 41] $k_{\rm ISC}$ (s ⁻¹)		
Molecule	$S_1 \leftrightarrow T_1$	$S_1 \leftrightarrow T_2$	$S_1 \rightarrow T_2$	$S_1 \rightarrow T_2$	$S_1 \rightarrow T_1$	$S_1\rightarrowT_2$	Total $k_{\rm ISC}$	Toluene ^b /film ^c
CzBO	0.155	-0.054	0.086	0.099	3.86×10^{6}	2.45×10^{5}	0.4×10^{7}	$-/2.5 \times 10^{7}$
CzBS	0.113	-0.146	0.381	0.527	5.79×10^{7}	4.74×10^{5}	0.6×10^{8}	$2.1 \times 10^8 / 1.9 \times 10^8$
CzRSe	0.095	-0.173	2.495	3 833	2.10×10^{9}	9.75×10^6	2.11×10^{9}	$1.28 \times 10^{9}/1.10 \times 10^{9}$

 $[^]a$ ΔE_{ST} and SOCME were calculated using the combined DFT-CCSD method considering PCM (toluene) solvent. b Experimental ISC rate in toluene. c Experimental ISC rate in film.

Table 6 Calculated singlet-triplet energy difference (ΔE_{ST}), spin-orbit coupling matrix element (SOCME), and RISC rate constants (k_{RISC}) for the CzBX series

	$\Delta E_{\rm ST}^{a}$ (eV)		$SOCME^a (cm^{-1})$		$k_{\text{RISC}} (s^{-1})$		Expt. [ref. 41] k_{RISC} (s ⁻¹)		
Molecules	$S_1\leftrightarrowT_1$	$S_1\leftrightarrowT_2$	$S_1 \leftarrow T_1$	$S_1 \leftarrow T_2$	$S_1 \leftarrow T_1$	$S_1 \leftarrow T_2 \leftarrow T_1^{d}$	Total $k_{\rm RISC}$	Toluene ^b /film ^c	
CzBO	0.155	-0.054	0.077	0.286	7.44×10^{3}	5.11×10^{3}	1.26×10^4	$-/9 \times 10^{3}$	
CzBS	0.113	-0.146	0.438	0.496	9.43×10^{5}	5.17×10^{3}	9.48×10^{5}	$4 \times 10^5/2.2 \times 10^5$	
CzBSe	0.095	-0.173	2.209	4.054	4.08×10^{7}	2.6×10^{5}	0.41×10^8	$1.5 \times 10^8/1.8 \times 10^8$	

 $[^]a$ $\Delta E_{\rm ST}$ and SOCME were calculated using the combined DFT-CCSD method considering the PCM (toluene) solvent. b Experimental ISC rate in toluene. c Experimental ISC rate in film. d The k_{RISC} values were calculated by taking into account the RISC from T_1 via T_2 to S_1 ; the relative population in the T_2 state with respect to that in the T_1 state was obtained by considering the thermal equilibrium (ref. 15).

chalcogen atoms (viz., 0.077, 0.438 and 2.209 cm⁻¹, respectively, between the S₁ and T₁ states, see Table 6 and Table S5, ESI†). The ISC rate for the CzBX series is calculated using eqn (2)-(4) and compared with the available experimental data.41 In this CzBX series of molecules, intramolecular H...H steric repulsions between the phenyl rings progressively increases, leading to the geometries becoming more puckered. This results in a twisted shape with heavy Se atoms, enhancing the spin-orbit coupling (SOC) and intersystem crossing rate (ISC and RISC) constants. The calculated ISC rate constants of CzBO and CzBS molecules are $4.0 \times 10^6 \text{ s}^{-1}$ and $6.0 \times 10^7 \text{ s}^{-1}$, respectively. The same for the heavy chalcogen atom Se substituted in the CzBSe molecule is $2.11 \times 10^9 \text{ s}^{-1}$ and the corresponding reported experimental data is $1.28 \times 10^9 \text{ s}^{-1}$. RISC is mostly favorable for this type of pure organic MR-TADF molecules. The k_{RISC} values were calculated by taking into account the RISC not only directly from T₁ to S₁ but also from T₁ to S₁ via the T₂ states. The relative population in the T₂ state with respect to that in the T₁ state was obtained by considering thermal equilibrium.15

The calculated rate constant of RISC for the CzBO molecule is $1.26 \times 10^4 \, \mathrm{s^{-1}}$, while the reported experimental value is $9.0 \times 10^3 \, \mathrm{s^{-1}}$ (in film). For the CzBS molecule, the calculated and experimentally reported RISC rate constants are $9.48 \times 10^5 \, \mathrm{s^{-1}}$ and $4.0 \times 10^5 \, \mathrm{s^{-1}}$, respectively. The heavy chalcogen atom Se substituted in the CzBSe molecule results in RISC rate constants of $0.41 \times 10^8 \, \mathrm{s^{-1}}$ (calc.) and $1.50 \times 10^8 \, \mathrm{s^{-1}}$ (exp.), respectively (see Table 6), which is the experimentally recorded high k_{RISC} in recent times. The presence of heavy atoms gradually increased the k_{RISC} due to an increase in SOCME. In the CzBX2X series, the molecules are categorized into two types, *i.e.*, planar and UCS shape. The excited state geometry of these planar shapes has a 0° to 1.2° dihedral angle for CzBO2S

(1.2°), CzBO2Se (0.4°), CzBS2S (0.1°), CzBS2Se, CzBSe2S and CzBSe2Se. The planar emitters have a very low SOCME, and in the presence of doubly substituted Se molecules with a high SOCME of above 0.088 cm⁻¹ compared to other (non-Se atom and single substituted Se) SOCME of less than 0.009 cm⁻¹ (except for CzBSe2S, 0.073 cm⁻¹). Similarly, the excited state geometry of UCS molecules is significantly increased (>0.09 cm⁻¹ due to the curve moiety). The dihedral angles of 20.8° (CzBO2O), 13.1° (CzBS2O), and 5.5° (CzBSe2Se) make the USC construction feasible, and the O atom has a shorter bond length with the nearest C atom distance (d(C-O) is \sim 1.37-1.4 Å), chalcogen has a longer bond length with the nearest C atom (C-O \sim 1.37-1.4 Å, C-S \sim 1.76 - 1.82 Å and C-Se \sim 1.92-1.99 Å), as shown in Table S6 (ESI†).

The UCS-shaped CzBO2O in the CzBO2X series has lower $\Delta E_{\text{S,-T,}}$ (= 0.043 eV) and comparatively higher SOCME (0.082 cm^{-1}) with a total ISC rate constant of $1.17 \times 10^6 \text{ s}^{-1}$. Similarly, for RISC, CzBO2O has a higher value of SOCME $(S_1 \leftarrow T_1 \text{ is } 0.091 \text{ and } S_1 \leftarrow T_2 \text{ is } 0.213 \text{ cm}^{-1}) \text{ and less energy}$ gap ($\Delta E_{S_1-T_1} = 0.043$, $E_{S_1-T_2} = -0.36$ eV), and the conversional total RISC rate constant is $2.70 \times 10^5 \,\mathrm{s}^{-1}$. The other two CzBO2S and CzBO2Se molecules are planar in nature due to the high S and Se atom distances, and the RMSD is also less than ~ 0.02 Å. The CzBO2S molecule has a lesser SOCME of 0.009 cm⁻¹ and a smaller energy gap ($\Delta E_{\mathrm{S_1-T_1}}$ = 0.028, $\Delta E_{\mathrm{S_1-T_2}}$ = -0.075 eV), and the rate of RISC is $1.13 \times 10^3 \text{ s}^{-1}$. The doubly substituted Se-based CzBO2Se molecule has a high SOCME (0.012 cm⁻¹ in $S_1 \leftarrow T_1$ and 0.085 cm⁻¹ in $S_1 \leftarrow T_2$) and increased the total $k_{\rm RISC}$ of 9.35 \times 10³ s⁻¹. In comparison, the CzBO2X series of rate ISC and RISC in CzBO2O, CzBO2O and CzBO2Se have high $k_{\rm ISC}$ (see Tables 7 and 8). In the CzBS2X series, the CzBS2O molecule, with a UCS, has less $\Delta E_{S_1-T_n}$ ($\Delta E_{S_1-T_1}$ is 0.137, $\Delta E_{S_1-T_2}$ is -0.196 eV) and high (in CzBS2X series only) SOCMEs **Paper PCCP**

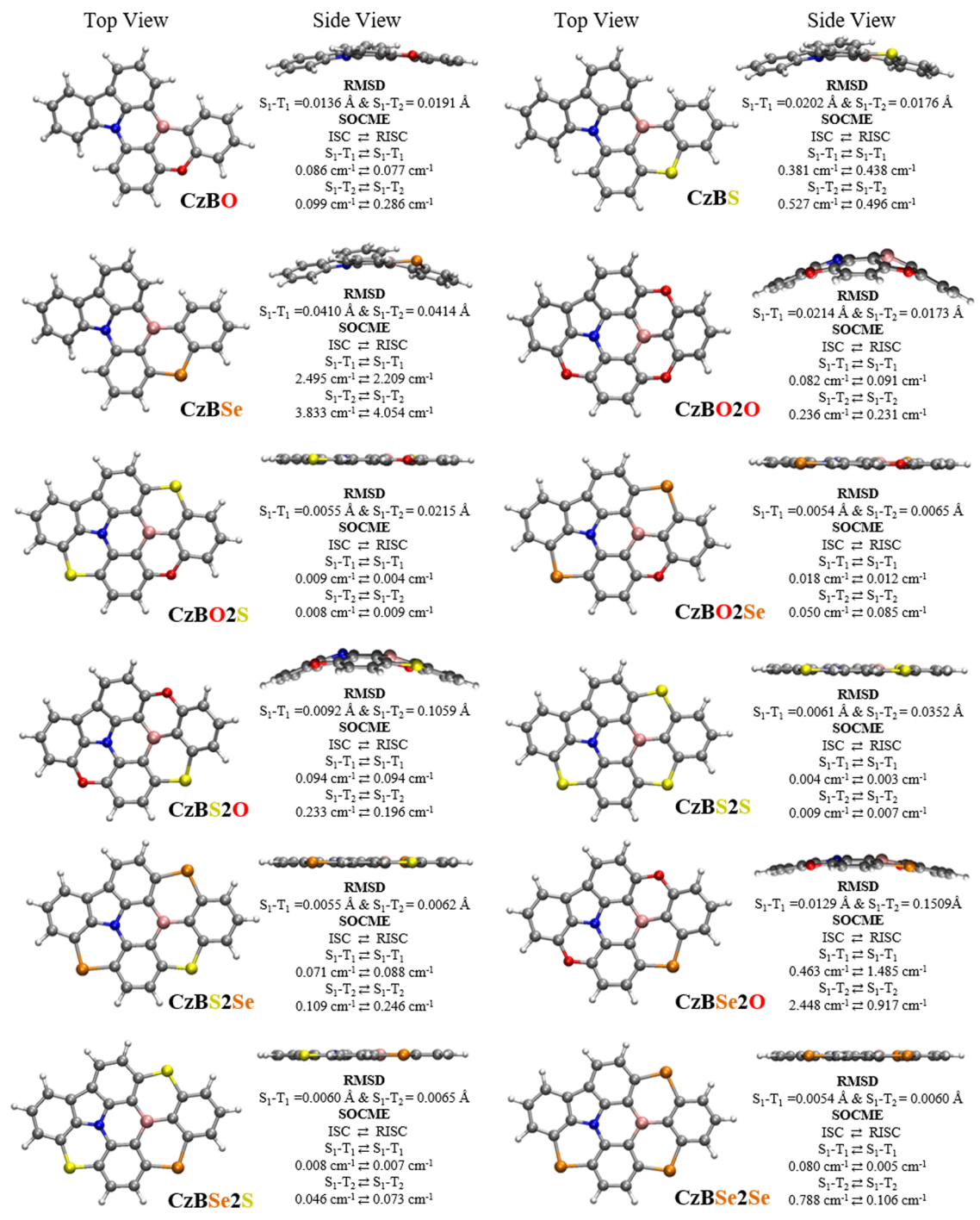


Fig. 4 The S_1 excited state structures of CzBX and CzBX2X. Excited state $(S_1/T_1/T_2)$ different chalcogens bond distances with carbon atom (d(X-C)) when X = O, S, or Se), collected in Table S6 (ESI†)

 $(S_1 \rightarrow T_1 \text{ is } 0.137 \text{ cm}^{-1} \text{ and } S_1 \rightarrow T_2 \text{ is } 0.233 \text{ cm}^{-1}); \text{ the}$ conversional total ISC rate reached $4.22 \times 10^6 \text{ s}^{-1}$. Similarly, for RISC, CzBS2O has a high SOCMEs ($S_1 \leftarrow T_1$ is 0.094 cm⁻¹ and $S_1 \leftarrow T_2$ is 0.196 cm⁻¹) and less ($\Delta E_{S_1-T_1} = 0.137$, $\Delta E_{S_1-T_2} = 0.137$ -0.196 eV) energy gap, and the total $k_{\rm RISC}$ reached 2.04 imes104 s⁻¹. The other two CzBS2S and CzBS2Se molecules are planar in nature. Also, these two molecules have low $\Delta E_{S_1-T_n}$ and SOCMEs; hence, their $k_{\rm ISC}$ becomes low as well as that of $\sim\!10^5~\text{s}^{-1}.$ The CzBS2S molecule has low SOC matrix elements $(S_1 \leftarrow T_1 \text{ is } 0.003 \text{ cm}^{-1} \text{ and } S_1 \leftarrow T_2 \text{ is } 0.007 \text{ cm}^{-1})$, a smaller energy gap ($\Delta E_{S_1-T_1} = 0.086$, $\Delta E_{S_1-T_2} = -0.129$ eV), and the rate of RISC is $1.02 \times 10^2 \text{ s}^{-1}$. For the **CzBS2Se** molecule, the heavy Se atom has a high SOCMEs ($S_1 \leftarrow T_1$ is 0.088 cm⁻¹ and $S_1 \leftarrow T_2$ is 0.246 cm⁻¹), which increased the k_{RISC} up to 2.41 \times 10⁵ s⁻¹.

The ISC and RISC rates went up a lot because of the heavy Se atoms in the CzBSe2X series and the molecule CzBSe2O, which

PCCP

Table 7 Calculated singlet-triplet energy difference (ΔE_{ST}), spin-orbit coupling matrix element (SOCME), and ISC rate constants (k_{ISC}) for **CzBX2X** molecules

	Calc. $\Delta E_{\rm ST}$ (e	V)	Calc. SOCME	c (cm ⁻¹)	$k_{\rm ISC} (s^{-1})$		
Molecules	$S_1 \leftrightarrow T_1$	$S_1 \leftrightarrow T_2$	$S_1\rightarrowT_1$	$S_1\rightarrowT_2$	$S_1 \rightarrow T_1$	$S_1 \rightarrow T_2$	Tot. $k_{\rm ISC}$ (s ⁻¹)
CzBO2O	0.043	-0.360	0.082	0.236	1.17×10^{6}	7.60×10^{0}	1.17×10^{6}
CzBO2S	0.028	-0.075	0.009	0.008	1.11×10^4	9.32×10^{2}	1.20×10^4
CzBO2Se	0.013	-0.239	0.018	0.050	$3.41 imes 10^4$	$1.22 imes 10^2$	3.42×10^{4}
CzBS2O	0.137	-0.196	0.094	0.233	$4.20 imes 10^6$	1.52×10^4	$4.22 imes 10^6$
CzBS2S	0.086	-0.129	0.004	0.009	4.90×10^{3}	2.42×10^{2}	$5.14 imes 10^3$
CzBS2Se	0.045	-0.275	0.071	0.109	9.03×10^{5}	1.17×10^{2}	9.04×10^{5}
CzBSe2O	0.207	-0.085	0.463	2.448	1.23×10^{8}	6.65×10^{7}	$1.90 imes 10^8$
CzBSe2S	0.090	-0.208	0.008	0.046	2.05×10^4	3.72×10^{2}	2.09×10^{4}
CzBSe2Se	0.058	-0.240	0.080	0.788	1.38×10^6	2.91×10^4	1.41×10^6

Table 8 Calculated singlet-triplet energy difference (ΔE_{ST}), spin-orbit coupling matrix element (SOCME), and RISC rate constants (k_{RISC}) for **CzBX2X** molecules

	Calc. $\Delta E_{\rm ST}$ (e	eV)	Calc. SOCME	E (cm ⁻¹)	$k_{\rm RISC}~({ m s}^{-1})$			
Molecules	$S_1 \leftrightarrow T_1$	$S_1 \leftrightarrow T_2$	$S_1 \leftarrow T_1$	$S_1 \leftarrow T_2$	$S_1 \leftarrow T_1$	$S_1 \leftarrow T_2 \leftarrow T_1$	Tot. k_{RISC} (s ⁻¹)	
CzBO2O	0.043	-0.360	0.091	0.213	2.70×10^{5}	1.17	2.70×10^{5}	
CzBO2S	0.028	-0.075	0.004	0.009	7.36×10^{2}	3.97×10^{2}	1.13×10^{3}	
CzBO2Se	0.013	-0.239	0.012	0.085	9.14×10^3	2.13×10^{2}	9.35×10^{3}	
CzBS2O	0.137	-0.196	0.094	0.196	2.03×10^{4}	5.43×10^{1}	2.04×10^4	
CzBS2S	0.086	-0.129	0.003	0.007	9.71×10^{1}	4.95	1.02×10^2	
CzBS2Se	0.045	-0.275	0.088	0.246	2.41×10^{5}	1.04×10^2	2.41×10^{5}	
CzBSe2O	0.207	-0.085	1.485	0.917	$4.03 imes 10^5$	2.96×10^{3}	4.06×10^{5}	
CzBSe2S	0.090	-0.208	0.007	0.073	4.73×10^{2}	2.93×10^{1}	5.02×10^2	
CzBSe2Se	0.058	-0.240	0.089	0.106	1.79×10^{5}	5.52×10^{1}	1.79×10^{5}	

has both UCS and heavy Se atoms. Among the CzBX2X series, CzBSe2O exhibited a high ISC rate due to its higher SOCMEs $(S_1 \rightarrow T_1 \text{ is } 0.463 \text{ cm}^{-1} \text{ and } S_1 \rightarrow T_2 \text{ is } 2.448 \text{ cm}^{-1}) \text{ value}$ and the lowest energy gap ($\Delta E_{S,-T_1} = 0.207$ eV and $\Delta E_{S,-T_2} =$ -0.085 eV). It reached a very high ISC rate constant of 1.9 \times 10⁸ s⁻¹. The RISC rate of CzBSe2O is the highest in the CzBX2O series, with a $k_{\rm RISC}$ of $4.06 \times 10^5 {\rm s}^{-1}$ due to its low energy gap and high SOC matrix elements ($S_1 \leftarrow T_1$ is 1.485 cm⁻¹ and $S_1 \leftarrow$ T₂ is 0.917 cm⁻¹). The other two molecules are planar with the heavy Se atom of CzBSe2S as the low energy gap and a low SOCMEs $(S_1 \rightarrow T_1 \text{ is } 0.008 \text{ cm}^{-1} \text{ and } S_1 \rightarrow T_2 \text{ is } 0.046 \text{ cm}^{-1})$ value to reach $k_{\rm ISC}$ of 2.09 \times 10⁴ s⁻¹. But the RISC rate in CzBSe2S (single Se and double S atom) is low SOCMEs (in $S_1 \leftarrow$ T_1 is 0.007 cm⁻¹ and $S_1 \leftarrow T_2$ is 0.073 cm⁻¹) value to achieve $5.02 \times 10^2 \text{ s}^{-1}$. The CzBSe2Se molecule with three Se atoms and planar geometry has lower rate (ISC and RISC) constants (see Tables 7 and 8). The CzBSe2Se molecule has a low energy gap ($\Delta E_{S_1-T_1} = 0.058$, $\Delta E_{S_1-T_2} = -0.240$ eV) and good SOC matrix elements ($S_1 \rightarrow T_2$ is 0.788 cm⁻¹) to increase the k_{ISC} up to $1.41 \times 10^6 \text{ s}^{-1}$. The rate of RISC also had good SOCMEs $(S_1 \leftarrow T_1 \text{ is } 0.089 \text{ and } S_1 \leftarrow T_2 \text{ is } 0.106 \text{ cm}^{-1}) \text{ to achieve the } k_{RISC}$ up to $1.79 \times 10^5 \text{ s}^{-1}$. The highest RISC rate constant for the CzBSe2Se molecule, as reported in a previous work by Pratik et al., 47,48 showed that increasing the chalcogen heavy Se atom greatly increases the RISC rate constants for nonplanar molecules, but in our study, due to the planar geometry $(0^{\circ}$ dihedral angle) with triple Se heavy atoms, the k_{RISC} becomes $\sim 10^5 \text{ s}^{-1}$.

The RISC values are higher for doubly substituted chalcogen atoms: $2.7 \times 10^5 \text{ s}^{-1}$, $2.04 \times 10^4 \text{ s}^{-1}$ and $4.06 \times 10^5 \text{ s}^{-1}$ for CzBO2O, CzBS2O and CzBSe2O, respectively, due to the UCS shape (high bond distance in C-Se and less bond distance in

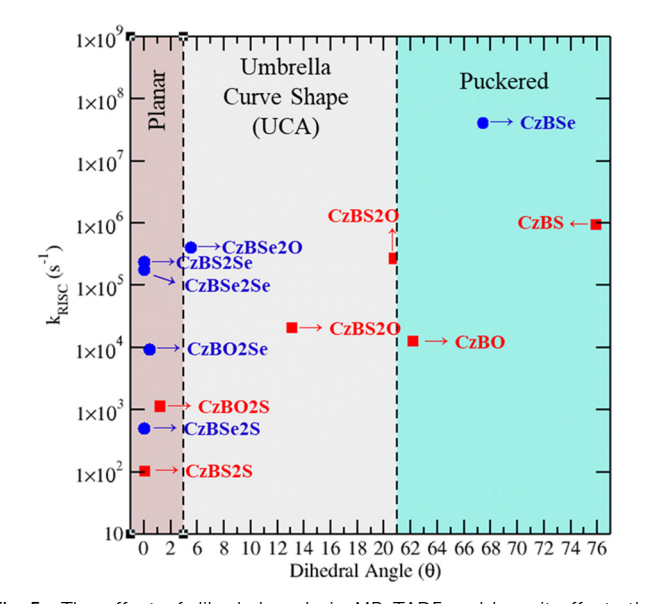


Fig. 5 The effect of dihedral angle in MR-TADF and how it affects the RISC rate constants in different shapes (planar (brown), UCS (grey) and puckered (turquoise)). Here, blue and red circles denote the molecules with and without Se atoms in both CzBX and CzBX2X

Paper

Comparison of the calculated rate constant for fluorescence ($k_{\rm F}$), ISC ($k_{\rm ISC}$) and RISC ($k_{\rm RISC}$) processes in s⁻¹ (here, ϕ is the dihedral angle in degrees)

		0				S				Se		
Molecules	ϕ (°)	$k_{\rm F} \left(10^7\right)$	$k_{\rm ISC} \left(10^7\right)$	$k_{\mathrm{RISC}} \left(10^4\right)$	ϕ (°)	$k_{ m F} \left(10^7 ight)$	$k_{\rm ISC} \left(10^7\right)$	$k_{ m RISC} \left(10^4\right)$	ϕ (°)	$k_{\rm F} \left(10^7\right)$	$k_{\rm ISC} \left(10^7\right)$	$k_{ m RISC} \left(10^5\right)$
CzBX (expt.) CzBX CzBO2X CzBS2X CzBSe2X	 62.2 20.8 13.1 5.5	15/13 17.4 11.4 12.2 14.2	/2.5 0.41 0.17 0.42 19	—/0.9 1.26 27 2.04 4.06	 75.9 1.2 0.1	1.5/3.3 15 9 9.24 8.62	$21/19$ 5.84 1.2×10^4 5.1×10^3 2.1×10^4	$40/22$ 94.8 0.13 1.02×10^{2} 5.02×10^{2}	 67.4 0.4 0	0.05 14.6 9.13 8.51 8.33	$ \begin{array}{c} 128/110 \\ 211 \\ 3.42 \times 10^4 \\ 0.09 \\ 0.14 \end{array} $	$ \begin{array}{c} 1500/1800 \\ 411 \\ 0.093 \\ 2.41 \\ 6.21 \times 10^2 \end{array} $

C-O, see Table S5 for the UCS, ESI†) moiety. The majority of heavy atom compounds in MR-TADF reached the k_{RISC} , which is approximately 10^{4-7} s⁻¹. 71-73 This study shows the lightest atom with UCS, resulting in a $k_{\rm RISC} \sim 10^5 {\rm s}^{-1}$ for the CzBX2O series. The natural transition orbitals (NTOs) presented in Fig. S2 (ESI†) shows the intramolecular charge transfer nature. The rate of emission can decide the path; taking a deep look into the $k_{\rm F}$ and $k_{\rm P}$ decides the best way of converting the exciton energy of $S_1 \rightleftharpoons T_n$ (ISC and RISC) to reach $\sim 100\%$ of IQE.

3.3.2 Dihedral angle vs. RISC rate constants. The dihedral angles of CzBX and CzBX2X series are calculated in the C-N-B-C middle part (see Fig. 4). The dihedral angle and SOCME are the major phenomena that enhance the RISC rate constants plotted in Fig. 5. The shapes of molecules are described using different layer colours. The planar (unsubstituted Se atom) structure, having lower SOCME values $\sim 0.009 \text{ cm}^{-1}$ (in S₁ \leftarrow T_1 and $S_1 \leftarrow T_2$, reached the RISC rate constants lower than 10³ s⁻¹. Similarly, the similar planar structure with Se atom molecules reached the highest RISC rate up to 10^3 – 10^5 s⁻¹ (CzBO2Se, CzBS2Se and CzBSe2Se), and the dihedral angle is 1.2° for CzBO2S (due to the O distance, see Table S5, ESI†) while CzBS2S is planar (see Fig. 4). The UCS structure has a high RISC rate constant due to the non-planar shape and dihedral angle of

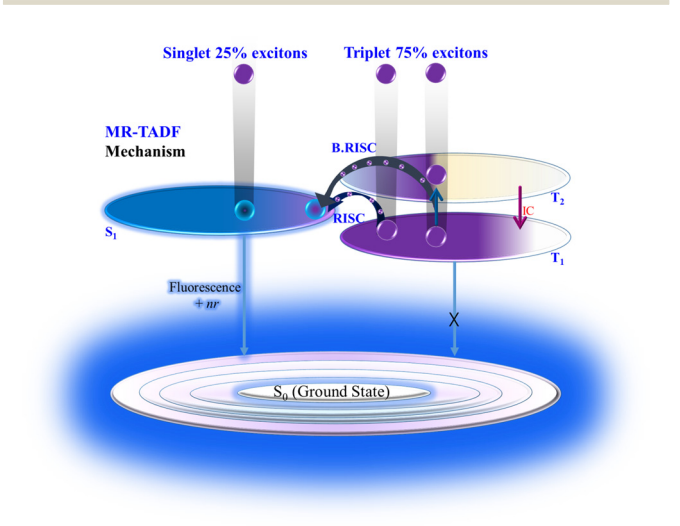


Fig. 6 MR-TADF mechanism in harvesting triplet excitons. Here B. RISC is T_1 to S_1 conversion via the T_2 state. The relative population in the T_2 state compared with the T₁ state was obtained by considering thermal equilibrium (using the Boltzmann factor).

20.8° for CzBO2O (triple O atom high dihedral angle in CzBX2X series), 13.1° for CzBS2O and 5.5° for CzBSe2O. These dihedral angles boosted the SOCME values and hence increased the RISC rate constants up to 10^4 – 10^5 s⁻¹. The main series of CzBX has a puckered shape and is twisted in the excited state; the dihedral angle also greatly increases in the 62°-76° range. High dihedral angle increases the SOCME and RISC rate constants up to $1.26 \times 10^4 \text{ s}^{-1}$ (CzBO), $9.48 \times 10^5 \text{ s}^{-1}$ (CzBS), and $0.41 \times 10^8 \text{ s}^{-1}(\text{CzBSe})$. The presence of heavy or metal atoms will significantly increase the intersystem rate constants (ISC and RISC), and SOCME always plays an important role in the twisted or bent shape of the structure.

The different rate constants of fluorescence (k_F) , ISC (k_{ISC}) and RISC (k_{RISC}) are compared in Table 9 (and Table S7, ESI†). Because of the higher rate constant for RISC compared to that of phosphorescence, these molecules show TADF features (see Fig. 6).

4. Conclusions

In conclusion, we investigated how chalcogens $(O \rightarrow S \rightarrow Se)$ affect the MR-TADF features and properties for a series of CzBX and CzBX2X molecules obtained either by the substitution of O atoms with S or Se in CzBX or by fusing intramolecular H...H bond with chalcogen atoms, the CzBX adjacent phenyl position to create the new MR-TADF CzBX2X series. The results of calculations based on highly correlated wave functions show the following.

- (i) The CzBX and CzBX2X series of MR-TADF emitters have high radiative (fluorescence) rate constants (k_F) of about $\sim 10^{7-8} \text{ s}^{-1}$.
- (ii) The ISC and RISC rate constants that follow are significantly influenced by the molecules electronic structure and geometry. While the CzBX series has the same chemical compositions, the ISC and RISC rate constants are found to be much larger due to the increasing chalcogen molecular size order (O \rightarrow S \rightarrow Se) compared to the CzBX2X series, which has lower SOCME values due to the planer and puckered geometry. UCS structures have higher SOCMEs.
- (iii) The selenium-containing (CzBX) molecules exhibit higher ISC and RISC rate values ($k_{\rm ISC} \sim 10^9 \ {\rm s}^{-1}$ and $k_{\rm RISC} \sim$ 10⁸ s⁻¹), which is due to the higher spin-orbit coupling interactions. The higher RISC rate constants in the CzBX2X series for both types of planar and UCS geometries reach $\sim 10^5 \text{ s}^{-1}$.

PCCP

(iv) The phosphorescence rate constants ($k_{\rm P}$) are in the range from $\sim 10^1$ to 10^4 s⁻¹ (calculated). Due to faster RISC and fluorescence rate constants, these **CzBX** and **CzBX2X** series of MR-TADF emitters show bright fluorescence ($k_{\rm F} \sim 10^{7-8}$ s⁻¹).

(v) This CzBX series of molecules has a unique deep-sky blue luminescence with sharp narrow band emission peaks and CzBX2X as bright bluish emitters.

Overall, we demonstrated that the chemical nature of the chalcogen atoms, as well as their changing position(s), have a significant influence on the optical and electronic features of the CzBX and CzBX2X-based MR-TADF emitters and their accurate prediction using combined DFT and CCSD methods. We compared our calculated results with available experimentally reported data to validate our computational methodology used in this study. We used PCM solvent (toluene) model to mimic the surrounding environment effect in the bulk. In reality, it is difficult to mimic the properties of thin films as the properties of any thin-film depend on its thickness. Here in, we explained the origins of MR-TADF properties in organoboron heteroatom-embedded molecules from the molecular point of view. We believe that the present methodology and findings will aid in the development of narrow-band blue OLED emitters with a high level of efficiency.

Author contributions

P. S.: conceptualization of the total work, computation and analysis of the works done, writing the original manuscript. P. K. S.: overall supervision, analysis and writing the manuscript.

Conflicts of interest

The authors declare no competing financial interest.

Acknowledgements

P. S. thanks BITS-Pilani for the "Institute Research Fellowship". P. K. S. thanks Department of Science and Technology-Science and Engineering Research Board (DST-SERB), Government of India (grant number: CRG/2021/002706) for the partial financial support. We acknowledge the support for high-performance computing and storage resources at GITAM and BITS-Pilani (Hyderabad Campus).

References

- 1 T. Wang, Y. Zou, Z. Huang, N. Li, J. Miao and C. Yang, *Angew. Chem., Int. Ed.*, 2022, **61**, 1–7.
- 2 H. Gao, S. Shen, Y. Qin, G. Liu, T. Gao, X. Dong, Z. Pang, X. Xie, P. Wang and Y. Wang, J. Phys. Chem. Lett., 2022, 13, 7561–7567.
- 3 S. Lin, Z. Pei, B. Zhang, H. Ma and W. Z. Liang, *J. Phys. Chem. A*, 2022, **126**, 239–248.
- 4 P. Jiang, J. Miao, X. Cao, H. Xia, K. Pan, T. Hua, X. Lv, Z. Huang, Y. Zou and C. Yang, Adv. Mater., 2022, 34, 1-7.

- 5 Y. C. Cheng, X. C. Fan, F. Huang, X. Xiong, J. Yu, K. Wang, C. S. Lee and X. H. Zhang, *Angew. Chem., Int. Ed.*, 2022, **61**, 1–6
- 6 X. Wu, J. Huang, B. Su, S. Wang, L. Yuan, W. Zheng, H. Zhang, Y. Zheng, W. Zhu and P. Chou, Adv. Mater., 2022, 34, 2270006.
- 7 G. Zhao, D. Liu, P. Wang, X. Huang, H. Chen, Y. Zhang, D. Zhang, W. Jiang, Y. Sun and L. Duan, *Angew. Chem., Int. Ed.*, 2022, **61**, e202212861.
- 8 J. Park, J. Lim, J. H. Lee, B. Jang, J. H. Han, S. S. Yoon and J. Y. Lee, *ACS Appl. Mater. Interfaces*, 2021, **13**, 45798–45805.
- 9 Y. Liu, X. Xiao, Z. Huang, D. Yang, D. Ma, J. Liu, B. Lei, Z. Bin and J. You, *Angew. Chem., Int. Ed.*, 2022, 134, e202210210.
- 10 N. Ikeda, S. Oda, R. Matsumoto, M. Yoshioka, D. Fukushima, K. Yoshiura, N. Yasuda and T. Hatakeyama, Adv. Mater., 2020, 32, 1–6.
- 11 W. Sotoyama, J. Phys. Chem. A, 2021, 125, 10373-10378.
- 12 S. Wu, W. Li, K. Yoshida, D. Hall, S. Madayanad Suresh, T. Sayner, J. Gong, D. Beljonne, Y. Olivier, I. D. W. Samuel and E. Zysman-Colman, ACS Appl. Mater. Interfaces, 2022, 14, 22314–22352.
- 13 H. Cheon, S. Woo, S. Baek, J. Lee and Y. Kim, *Adv. Mater.*, 2022, 34, 2207416.
- 14 P. K. Samanta and N. J. English, J. Phys. Chem. C, 2020, 124, 8178–8185.
- 15 P. K. Samanta, D. Kim, V. Coropceanu and J. L. Brédas, J. Am. Chem. Soc., 2017, 139, 4042–4051.
- 16 B. C. Garain, P. K. Samanta and S. K. Pati, J. Phys. Chem. A, 2021, 125, 6674–6680.
- 17 S. Kuila, A. Ghorai, P. K. Samanta, R. B. K. Siram, S. K. Pati, K. S. Narayan and S. J. George, *Chem. – Eur. J.*, 2019, 25, 16007–16011.
- 18 H. Shu, L. Chen, X. Wu, T. Wang, S. Wang, H. Tong and L. Wang, J. Mater. Chem. C, 2022, 10, 1833–1838.
- 19 B. Li, Z. Yang, W. Gong, X. Chen, D. W. Bruce, S. Wang, H. Ma, Y. Liu, W. Zhu, Z. Chi and Y. Wang, *Adv. Opt. Mater.*, 2021, 9, 1–10.
- 20 P. Sivasakthi, J. M. Jacob, M. K. Ravva and P. K. Samanta, J. Phys. Chem. A, 2022, 124, 886–893.
- 21 A. Arjona-Esteban, S. Barbara and O. Julian, *Lumin. OLED Technol. Appl.*, 2019, 1–18.
- 22 D. K. A. Phan Huu, S. Saseendran, R. Dhali, L. G. Franca, K. Stavrou, A. Monkman and A. Painelli, *J. Am. Chem. Soc.*, 2022, 144, 15211–15222.
- 23 R. Dhali, D. K. A. Phan Huu, F. Terenziani, C. Sissa and A. Painelli, *J. Chem. Phys.*, 2021, **154**, 134112.
- 24 M. Li, W. Xie, X. Cai, X. Peng, K. Liu, Q. Gu, J. Zhou, W. Qiu, Z. Chen, Y. Gan and S. J. Su, *Angew. Chem., Int. Ed.*, 2022, 61, e202209343.
- 25 A. Chatterjee, J. Chatterjee, S. Sappati, T. Sheikh, R. M. Umesh, M. D. Ambhore, M. Lahiri and P. Hazra, *J. Phys. Chem. B*, 2021, 125, 12832–12846.
- 26 Kenry, C. Chen and B. Liu, Nat. Commun., 2019, 10, 1-15.
- 27 J. Yu, H. Ma, W. Huang, Z. Liang, K. Zhou, A. Lv, X.-G. Li and Z. He, *JACS Au*, 2021, 1, 1694–1699.
- 28 P. K. Samanta and S. K. Pati, J. Mol. Model., 2018, 24, 1-11.

Paper

- 29 N. Liang, G. Liu, D. Hu, K. Wang, Y. Li, T. Zhai, X. Zhang, Z. Shuai, H. Yan, J. Hou and Z. Wang, Adv. Sci., 2022, 9, 2103975.
- 30 R. K. Konidena and K. R. Naveen, Adv. Photonics Res., 2022, 3, 2200201.
- 31 K. R. Naveen, P. Palanisamy, M. Y. Chae and J. H. Kwon, Chem. Commun., 2023, 59, 3685-3702.
- 32 T. Wang, A. K. Gupta, D. B. Cordes, A. M. Z. Slawin and E. Zysman-Colman, Adv. Opt. Mater., 2023, 11, 2300114.
- 33 T. Hatakeyama, K. Shiren, K. Nakajima, S. Nomura, S. Nakatsuka, K. Kinoshita, J. Ni, Y. Ono and T. Ikuta, Adv. Mater., 2016, 28, 2777-2781.
- 34 S. Madayanad Suresh, D. Hall, D. Beljonne, Y. Olivier and E. Zysman-Colman, Adv. Funct. Mater., 2020, 30, 1908677.
- 35 S. Oda, W. Kumano, T. Hama, R. Kawasumi, K. Yoshiura and T. Hatakeyama, Angew. Chem., 2021, 133, 2918-2922.
- 36 K. R. Naveen, H. I. Yang and J. H. Kwon, Commun. Chem., 2022, 5, 149.
- 37 S. Oda, T. Sugitani, H. Tanaka, K. Tabata, R. Kawasumi and T. Hatakeyama, Adv. Mater., 2022, 34, 1-6.
- 38 K. R. Naveen, H. Lee, L. H. Seung, Y. H. Jung, C. P. Keshavananda Prabhu, S. Muruganantham and J. H. Kwon, Chem. Eng. J., 2023, 451, 138498.
- 39 P. Palanisamy, O. P. Kumar, H. U. Kim, K. R. Naveen, J. Y. Kim, J. H. Baek, M. Y. Chae and J. H. Kwon, Chem. Eng. J., 2024, 481, 148781.
- 40 H. X. Ni, X. F. Luo, L. Yuan, J. J. Hu, W. W. Zhang and Y. X. Zheng, J. Mater. Chem. C, 2024, 12, 2578-2584.
- 41 I. S. Park, H. Min and T. Yasuda, Angew. Chem., Int. Ed., 2022, 134, e202205684.
- 42 M. Yang, I. S. Park and T. Yasuda, J. Am. Chem. Soc., 2020, **142**, 19468-19472.
- 43 Y. Zhang, D. Zhang, J. Wei, Z. Liu, Y. Lu and L. Duan, Angew. Chem., Int. Ed., 2019, 58, 16912-16917.
- 44 K. Matsui, S. Oda, K. Yoshiura, K. Nakajima, N. Yasuda and T. Hatakeyama, J. Am. Chem. Soc., 2018, 140, 1195-1198.
- 45 H. Hirai, K. Nakajima, S. Nakatsuka, K. Shiren, J. Ni, S. Nomura, T. Ikuta and T. Hatakeyama, Angew. Chem., Int. Ed., 2015, 54, 13581-13585.
- 46 H. Jiang, Y. Cao, Q. Yang, L. Xian, Y. Tao, R. Chen and W. Huang, J. Phys. Chem. Lett., 2020, 11, 7739-7754.
- 47 S. M. Pratik, V. Coropceanu and J. L. Brédas, *Chem. Mater.*, 2022, 34, 8022-8030.
- 48 S. M. Pratik, V. Coropceanu and J. L. Brédas, ACS Mater. Lett., 2022, 4, 440-447.
- 49 H. Sun, C. Zhong and J. L. Brédas, J. Chem. Theory Comput., 2015, 11, 3851-3858.
- 50 M. Rubešová, E. Muchová and P. Slavíček, J. Chem. Theory Comput., 2017, 13, 4972-4983.
- 51 G. Scalmani and M. J. Frisch, J. Chem. Phys., 2010, 132, 114110.
- 52 S. Rohman and R. Kar, J. Phys. Chem. A, 2022, 126, 3452-3462
- 53 O. S. Bokareva, G. Grell, S. I. Bokarev and O. Kühn, J. Chem. Theory Comput., 2015, 11, 1700-1709.
- 54 L. Kronik, T. Stein, S. Refaely-Abramson and R. Baer, J. Chem. Theory Comput., 2012, 8, 1515-1531.

- 55 M. J. Frisch, G. W. Trucks, H. B. Schlegel, G. E. Scuseria, M. A. Robb, J. R. Cheeseman, G. Scalmani, V. Barone, G. A. Petersson, H. Nakatsuji, X. Li, M. Caricato, A. V. Marenich, J. Bloino, B. G. Janesko, R. Gomperts, B. Mennucci, H. P. Hratchian, J. V. Ortiz, A. F. Izmaylov, J. L. Sonnenberg, D. Williams-Young, F. Ding, F. Lipparini, F. Egidi, J. Goings, B. Peng, A. Petrone, T. Henderson, D. Ranasinghe, V. G. Zakrzewski, J. Gao, N. Rega, G. Zheng, W. Liang, M. Hada, M. Ehara, K. Toyota, R. Fukuda, J. Hasegawa, M. Ishida, T. Nakajima, Y. Honda, O. Kitao, H. Nakai, T. Vreven, K. Throssell, J. A. Montgomery, Jr., J. E. Peralta, F. Ogliaro, M. J. Bearpark, J. J. Heyd, E. N. Brothers, K. N. Kudin, V. N. Staroverov, T. A. Keith, R. Kobayashi, J. Normand, K. Raghavachari, A. P. Rendell, J. C. Burant, S. S. Iyengar, J. Tomasi, M. Cossi, J. M. Millam, M. Klene, C. Adamo, R. Cammi, J. W. Ochterski, R. L. Martin, K. Morokuma, O. Farkas, J. B. Foresman and D. J. Fox, Gaussian 16, Revision C.02, Gaussian, Inc., Wallingford CT, 2016.
- 56 A. Pershin, D. Hall, V. Lemaur, J. C. Sancho-Garcia, L. Muccioli, E. Zysman-Colman, D. Beljonne and Y. Olivier, Nat. Commun., 2019, 10, 597.
- 57 F. Neese, F. Wennmohs, U. Becker and C. Riplinger, J. Chem. Phys., 2020, 152, 224108.
- 58 F. Neese, Wiley Interdiscip. Rev.: Comput. Mol. Sci., 2022, 12, e1606.
- 59 F. Weigend and R. Ahlrichs, Phys. Chem. Chem. Phys., 2005, 7, 3297-3305.
- 60 A. K. Dutta, M. Nooijen, F. Neese and R. Izsák, J. Chem. Phys., 2017, 146, 074103.
- 61 V. Lawetz, G. Orlandi and W. Siebrand, J. Chem. Phys., 1972, 56, 4058-4072.
- 62 G. W. Robinson and R. P. Frosch, J. Chem. Phys., 1963, 38, 1187-1203.
- 63 K. Schmidt, S. Brovelli, V. Coropceanu, D. Beljonne, J. Cornil, C. Bazzini, T. Caronna, R. Tubino, F. Meinardi, Z. Shuai and J. L. Brédas, J. Phys. Chem. A, 2007, 111, 10490-10499.
- 64 R. C. Hilborn, Am. J. Phys., 1982, 50, 982-986.
- 65 E. Jansson, B. Minaev, S. Schrader and H. Ågren, Chem. Phys., 2007, 333, 157-167.
- 66 Q. Zhang, X. Wang, Y. Zhang, L. Wang, J. Li and J. Zhang, J. Phys. Chem. C, 2016, 120, 27523-27532.
- 67 Z. Shuai and Q. Peng, Phys. Rep., 2014, 537, 123-156.
- 68 M. T. do Casal, K. Veys, M. H. E. Bousquet, D. Escudero and D. Jacquemin, J. Phys. Chem. A, 2023, 127, 10033-10053.
- 69 A. Manian and S. P. Russo, Sci. Rep., 2022, 12, 21481.
- 70 M. H. E. Bousquet, T. V. Papineau, K. Veys, D. Escudero and D. Jacquemin, J. Chem. Theory Comput., 2023, 19, 5525–5547.
- 71 X. Cao, K. Pan, J. Miao, X. Lv, Z. Huang, F. Ni, X. Yin, Y. Wei and C. Yang, J. Am. Chem. Soc., 2022, 144, 22976-22984.
- 72 S. Wu, L. Zhang, J. Wang, A. Kumar Gupta, I. D. W. Samuel and E. Zysman-Colman, Angew. Chem., Int. Ed., 2023, 62, e202305182.
- 73 T. Wang, A. K. Gupta, D. B. Cordes, A. M. Z. Slawin and E. Zysman-Colman, Adv. Opt. Mater., 2023, 11, 2300114.